A low-power prototype of contactless field power controlled BLAC and BLDC motors

Umesh Kumar Soni 🔟 and Ramesh Kumar Tripathi

Department of Electrical Engineering, MNNIT Allahabad, Prayagraj, UP 211004, India

CAMBRIDGE
UNIVERSITY PRESS

Abstract

In this paper, a new design configuration has been proposed in which a prototype of resonant inductive power transfer-based contactless power transfer to wound rotor has been developed which provides field power to brushless alternating current (BLAC) or brushless direct current (BLDC) motors without the use of permanent magnets in the rotor. Further, wound field in the rotor of DC motor can be powered without carbon brushes. The proposed design facilitates motor performance improvement by adding an extra dimension of field flux control, while the armature circuit is conventionally fed from position detection and commutation schemes. It contains a primary multilayer concentrated coil fed with high-frequency resonating AC supply or switched mode supply. A single layer helical secondary coil coaxially fixed on the shaft receives high frequency wireless AC power transmitted from primary coil. Fast rectifier inside the hollow shaft and DC filter provides the transferred DC power to field terminals in the rotor. It has been verified that rotor power can be varied linearly with linear variation in input DC power with the highest efficiency at the resonant frequency. Available power to the rotor remains invariable with rotational speed and angle, which is a necessary requirement for rotor field. DC voltage on the rotor terminals can be effectively controlled during standstill as well as during rotation at any speed.

Introduction

Slip rings and carbon brushes are the conventional solutions to transfer electrical power to the rotor circuit of electrical machines [1]. However, accumulation of conductive metallic dust between the slip-rings may introduce the arc due to the short circuit during operation [2] which is hazardous to the environment [3, 4]. Speed sensitivity and mechanical wear and tear affect the reliability of the brush/slip ring system. Later on, permanent magnets were preferred as rotor field to avoid these problems. Brushless AC (BLAC) and brushless DC (BLDC) with permanent magnet field have been used in large scale in industries, electric vehicles, medical implants and domestic purposes. Permanent magnets use rare earth material and now its demand is exceeding the supply [5]. They have limited mechanical strength and limited flux capacity. Brushless and permanent magnet-free wound rotor field controlled motors may prove potentially beneficial over interior permanent magnet synchronous motors and permanent magnet brushless DC (PMBLDC) motors as they can provide efficient and loss minimized field control [6]. Moreover, they impart identical performance characteristics with their PM counterparts. Controllable rotor field intensity can provide flux weakening control to attain the speed above the base speed. A design with two independent machines [7] connected through common shaft generates very low-frequency AC power which is later fed to DC field in the rotor through rotating rectifier in the shaft. However, DC field power depends on the shaft speed and it is zero at standstill. The strategy which can provide the contactless rotor power at standstill is essential. Rotating transformer was proposed as an alternative to non-contact replacement to transfer power from rotating photovoltaic panels to a satellite [8]. Well-established traditional rotary transformers were operated at the line frequency and demonstrated the efficiency of more than 90% with reduced cost [9–18]. However, extra system dynamics (L/R time constant) are involved in rotating transformers and brushless exciters. Different approaches were proposed to improve the factors such as core geometry, magnetic coupling structure, windings layout, amount of leakage inductance, inductors' misalignment, and thermal resistances [10, 19–23]. U-shaped core with a single part of primary winding was proposed [24]. An improved U-shaped and toroid-shaped geometry for a rotating transformer core was implemented in [25]. Power transfer to the rotor using coaxial solenoidal coils with axial separation, radial separation and flat face-to-face constructions were discussed in [26, 27].

In the proposed design, the permanent magnet field of BLAC and BLDC motor has been assumed to be replaced with that of wound field poles in the rotor fed from contactless power. With this construction, field flux control for high power and load applications can be facilitated. Out of two helical windings, one is in rotor shaft free to rotate and other is fixed concentrically and is stationary. Both coaxial windings are radically separated with a radial gap. The complete system has voltage source inverter (VSI)/current source inverter (CSI) which
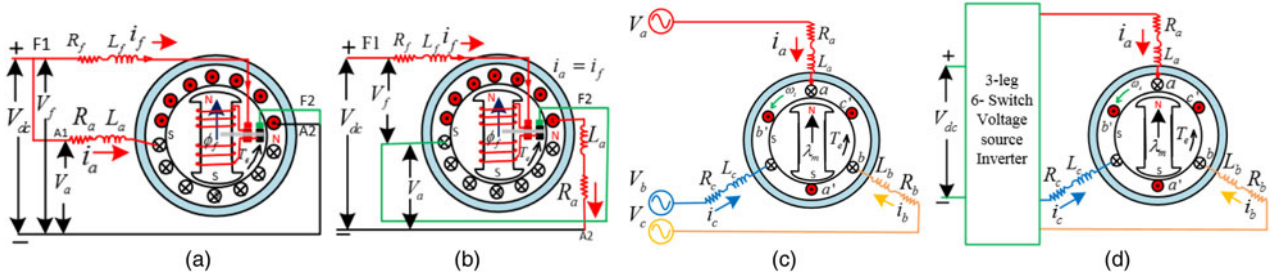
Fig. 1. (a) Shunt (or separately excited) construction of DC motor with the field in the rotor, (b) series configuration of DC motor with the field in the rotor, (c) BLAC (or PMSM), and (d) BLDC motor.

are commutated through the hall sensor, encoder or sensorless methods. The stator winding of the motor has the same configuration as in the previous designs of permanent magnet BLAC/BLDC motors. The proposed scheme is simple and works at standstill also unlike other schemes. Additionally, the resonant converters can be designed to operate at high efficiency. The step-by-step development of the proposed system has been discussed in the next sections.

Dependency of torque and speed in field flux

The typical circuit diagram of DC shunt (or separately excited) and series motor has been illustrated in Figs 1(a) and 1(b). Circuit diagram of BLAC and BLDC motor has been shown in Figs 1(c) and 1(d). In the shunt and separately excited DC motor, the developed electromagnetic torque is proportional to the field flux which depends on the current driven by the field circuit. The field current varies linearly with the field voltage for fixed DC resistance of field winding.

The electromagnetic torque developed in separately excited (or shunt) DC motor depends on the field resistance, field voltage, and armature current, while the speed of motor depends on armature resistance, field resistance, field voltage, armature voltage, and armature current. These relationships can be defined by equations (1) and (2) as given below,

$$T_e = K_T \phi_f i_a = K_T K_f i_f i_a = K_t . \frac{V_f}{R_f} . i_a, \tag{1}$$

$$N = \frac{V_a - i_a R_a}{K_T \phi_f} = \frac{V_a - i_a R_a}{K_T K_f i_f} = \frac{V_a - i_a R_a}{K_T K_f . V_f / R_f}. \tag{2}$$

Similarly, the torque and speed of series DC motor can be given by,

$$T_e = K_T \phi_f . i_a = K_T K_f i_f^2 = K_t . \left(\frac{V_f}{R_f} \right)^2. \tag{3}$$

Here, $K_t = K_T . K_f$ is a constant.

$$N = \frac{V_a - i_f (R_a + R_f)}{K_T \phi_f} = V_a \frac{R_f}{K_T K_f V_f} - \frac{1}{K_T K_f} (R_a + R_f), \tag{4}$$

where ϕ_f is useful field flux per pole in DC machine; K_T is torque constant and is equal to $K_T = Z.P/2\pi A$ for P number of poles, Z number of conductors, and A number of parallel paths; K_f is a constant; R_a is armature resistance; R_f is field resistance.

The electromagnetic torque of trapezoidal back EMF BLDC motor is given by,

$$T_e = \frac{P \psi_f}{2} \left[Trapez(\theta_r) i_a(t) + Trapez \left(\theta_r - \frac{2\pi}{3} \right) i_b(t) \right.$$
$$\left. + Trapez \left(\theta_r + \frac{2\pi}{3} \right) i_c(t) \right]. \tag{5}$$

Here, ψ_f is the total flux linkage of field. The quantities, $i_a(t)$, $i_b(t)$, and $i_c(t)$ are the phase currents in the stator winding of the BLDC motor. $Trapez(\theta_r)$ is a unity peak Trapezoidal function with 120° flat top.

Permanent magnet synchronous motor (PMSM) is BLAC motor with sinusoidal back EMF waveform and the torque equation for this motor can be given by,

$$T_e = \frac{3}{2} \frac{P}{2} [\lambda_d i_q - \lambda_q i_d]. \tag{6}$$

Here, λ_d is direct axis flux linkage due to phase energization and rotor field. λ_q is quadrature flux linkage. i_q is quadrature component of three-phase armature currents and i_d is the direct component of three-phase armature current.

$$\lambda_d = \lambda_m + L_d i_d, \tag{7}$$

$$\lambda_q = L_q i_q. \tag{8}$$

Here, λ_m is magnetic flux linkage due to the permanent magnet field. L_d is the equivalent inductance of armature winding in direct axis and L_q is the equivalent inductance of armature winding in quadrature axis. After replacing the values of λ_d and λ_q from equations (7) and (8) into (6) and simplifying, the resulting equation for electromagnetic torque of PMSM can be given as,

$$T_e = \frac{3}{2} \frac{P}{2} [\lambda_m i_q + (L_d - L_q) i_d i_q]. \tag{9}$$

Here, P is the number of poles. If field flux linkage λ_m is controlled by field current ($\lambda_m = M_d i_f$) unlike constant flux linkage in permanent magnets, the electromagnetic torque developed in the motor can be given by equation (10).

$$T_e = \frac{3}{2} \frac{P}{2} [M_d i_f i_q + (L_d - L_q) i_d i_q]. \tag{10}$$

Here, M_d is direct axis mutual inductance between field and armature.

Total field flux linkage ψ_f is the sum of flux linkages due to field current i_f and flux linkage due to direct axis current component i_d of armature currents and it is given by,

$$\psi_f = L_f i_f + M_d i_d. \tag{11}$$

Here, L_f is self-inductance of field winding. The field flux weakening is required for high-speed applications. However, in the PMBLDC motor and permanent magnet synchronous with the field in the rotor, the control of the flux linkage of the magnet is not possible. It is conventionally done by demagnetization; in which, flux opposite to field flux is generated by controlling the magnitude of direct axis component i_d of three-phase stator currents. Motor torque is reduced in this process.

If the field flux linkage could be directly controlled by varying the field current i_f, then it is not required to control the d-axis current component i_d for field weakening control. After the elimination of the direct axis component of flux linkage from equation (11), the field flux linkage can be given by,

$$\psi_f = L_f i_f. \tag{12}$$

The voltage equation for the field circuit can be given by,

$$v_f = r_f i_f + \frac{d\psi_f}{dt}. \tag{13}$$

In case of steady-state condition of field circuit, the second term in equation (13) can be ignored and field current i_f only depends on field voltage and field resistance. Further, in case of cylindrical (non-salient) rotor, direct axis inductance L_d is equal to quadrature axis inductance L_q. The resulting equation for variable electromagnetic torque can be given as,

$$T_e = \frac{3}{2}\frac{P}{2}\left[M_d \frac{V_f}{R_f} i_q\right]. \tag{14}$$

It can be understood from equation (14) that the electromagnetic torque developed by the synchronous motor can be changed by variation in the field voltage V_f applied to the field winding. Similarly, the torque equation of BLDC motor can be derived by substituting the values of field flux linkage from equation (12) and steady-state field current from equation (13) into (5).

$$T_e = \frac{P.L_f V_f}{2R_f}\left[Trapez(\theta_r)i_a(t) + Trapez\left(\theta_r - \frac{2\pi}{3}\right)i_b(t)\right. \\ \left. + Trapez\left(\theta_r + \frac{2\pi}{3}\right)i_c(t)\right]. \tag{15}$$

In case of constant power application, speed of the motor can be increased with a corresponding reduction in electromagnetic torque by field flux weakening which is achieved by reduced field voltage as observed from equations (14) and (15). However, the rotor voltage variation needs the carbon brushes involving brush drop. To solve this issue, wound rotor brushed construction (Fig. 1(a)) or the permanent magnet rotor construction (Fig. 1(b)) is replaced by contactless power fed wound rotor field as shown in Fig. 2. The wireless power available in the rotor terminals can be used for field flux control.
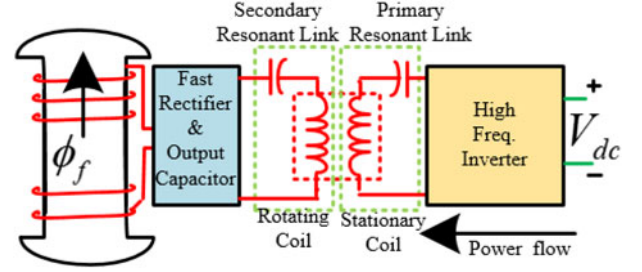

Fig. 2. Contactless power fed wound rotor field using the IPT.

Principle of contactless power transfer

Contactless power transfer (CPT), also called WPT, has been mostly used for delivery of power without conventional wires to avoid inconvenience and hazards [28, 29]. There are a number of well-established CPT technologies such as inductive power transfer (IPT), magnetic resonance power transfer, capacitive power transfer (CPT), microwave power transfer, acoustic power transfer and laser power transfer [30–33]. Among these, IPT, i.e. magnetic coupling-based wireless power transfer, has been the well-known technology for CPT in which the primary and the secondary windings of a conventional transformer are wound on isolated magnetic cores [34]. Recently, number of ways have been introduced to enhance the efficiency of contactless power transfer [35–40]. Different types of topologies were studied and compared [37]. Using the compensation capacitors in the circuits, is most common way to improve the efficiency. Based on the location of the inductors relative to capacitors in the circuits, four topologies exist such as parallel-parallel (pp), parallel-series (ps), series-series (ss), series-parallel (sp) topologies [38, 40]. The selection of the topologies depends on the field of application [41].

Resonant IPT-based basic series-series (SS) system for the proposed scheme of CPT facility to rotor field has been shown in Fig. 3(a). The equivalent circuit of the system has been given in Fig. 3(b). The high-frequency rectangular wave AC source is generated by a class-D full-bridge inverter whose dc input voltage is V_{dc}. V_p is the amplitude of the output voltage of the inverter; C_p, L_p and R_p are the capacitance, inductance and ESR of the primary resonant circuit respectively. The ESR of the capacitor is commonly small in comparison with that of the coil and may be ignored. V_s is output AC voltage of receiver coil. C_s, L_s and R_s are the capacitance, inductance and ESR of the secondary resonant circuit respectively. The field winding load resistance at the receiving loop is R_F and the mutual inductance is M, coupling coefficient between two coils is k. Primary and secondary parameters are assumed equal. The Fourier series expressions of the primary instantaneous voltage $V_p(t)$ (inverter output) and current $I_p(t)$ are given in equations (16) and (17) respectively [42],

$$v_p(t) = \sum_{n=1,3,5}^{\infty} \frac{4V_{dc}}{\pi n} \sin n\omega t, \tag{16}$$

$$i_p(t) = \sum_{n=1,3,5}^{\infty} \frac{4V_{dc}}{\pi n|Z_T|} \sin\left(n\omega t - \phi_z\right). \tag{17}$$

Here, ϕ_z is the phase angle of the load having total impedance Z_T seen from the output of H-bridge inverter and ω is operating frequency in rad/sec.
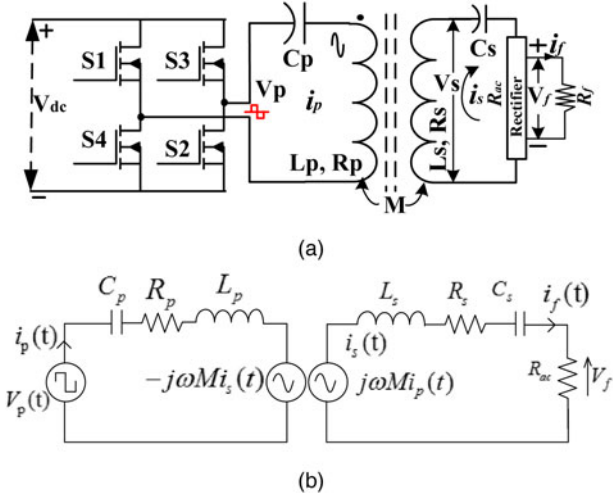
Fig. 3. (a) Basic series-series resonant IPT system. (b) Equivalent circuit referred to the transmitter side.

The total impedance is the sum of primary impedance and secondary referred impedance given by,

$$Z_T = Z_p + Z_{sr}. \tag{18}$$

The expression for total n^{th} harmonic impedance from the equivalent circuit of Fig. 3(b),

$$Z_T = R_p + j\left(n\omega L_p - \frac{1}{n\omega C_p}\right)$$
$$+ \frac{(n\omega M)^2}{R_s + j(n\omega L_s - 1/n\omega C_s) + R_{ac}}, \tag{19}$$

where mutual inductance M is given by $M = k\sqrt{L_p L_s}$. When the mutual inductance of the coils is low, a lower voltage is induced in the receiver coil and the efficiency is low. However, for the low value of M, the output voltage at the receiver end can be increased by increasing the transmitter current I_p which is maximum at resonating frequency of the transmitter circuit. I_p may decrease due to a detuned transmitter. R_{ac} is the effective load resistance, seen from the input side of the rectifier and the optimum value of R_{ac} in terms of R_f is given by,

$$R_{ac} = \frac{\pi^2}{8} R_f. \tag{20}$$

The inductance of multilayer helical winding of the secondary is calculated [43] from,

$$L_s = \frac{\mu \pi D^2 N_s^2}{4h}, \tag{21}$$

where μ is the relative permeability of vacuum, D is the diameter of the coil, N_s is the number of turns in the secondary coil and h is the length of the coil. The induced voltage in the secondary coil is given as [43],

$$v_s(t) = \frac{d\phi}{dt} = M\frac{di_p(t)}{dt} = M\omega I_p \cos(\omega t). \tag{22}$$

The relation between the currents i_p, i_{ac} and V_p can be rgiven by,

$$i_{ac} = \frac{j\omega M}{Z_s} i_p, \tag{23}$$

$$i_p = \frac{V_p}{Z_p + \omega^2 M^2/Z_s}. \tag{24}$$

The efficiency of IPT using SS compensation network at primary resonance frequency is given by [44],

$$\eta = \frac{P_{load}}{P_p} = -\frac{\text{Re}[V_{ac}, I_{ac}^*]}{\text{Re}[V_p, I_p^*]}$$
$$= \frac{R_{ac}}{((R_{ac} + R_s) + R_P((\omega L_s - 1/\omega C_s)^2 + (R_S + R_{ac})^2)/\omega^2 M^2)}. \tag{25}$$

Efficiency reaches high when the resonant circuit operates at the resonant frequency of input LC circuit. Reactive terms do not appear in equation (25) [43]

$$\eta = \frac{R_{ac}}{(R_{ac} + R_s)(1 + R_P(R_S + R_{ac})/\omega^2 M^2)}. \tag{26}$$

In terms of factor γ derived from quality factors, the efficiency can be given by,

$$\eta_{\max} = \left(\frac{\gamma}{1 + \sqrt{1 + \gamma^2}}\right)^2, \tag{27}$$

where $\gamma = k\sqrt{Q_p.Q_s}$ comprises of the coupling coefficient with the quality factors Q_p and Q_s of the primary and secondary coil [45]. It can be concluded from equation (27) that maximum efficiency can be increased by increasing the quality factors. This can be achieved through the adjustment of load resistance, i.e. field winding resistance. The circuit arrangement for the proposed scheme of controlling the rotor circuit voltage has been shown in Fig. 4(a). In this scheme, the high-frequency resonant inverter is used to transmit the power over the wireless channel. Close-loop controlled DC-DC converter provides variable DC supply to the resonant inverter operating at optimized resonance frequency as shown in Fig. 4(b). V'_{dc} is the input to DC-DC converter. V_{dc} is the actual voltage at the input terminals of the resonant converter. V_{ref} is the reference voltage required for developing the certain rotor field flux.

In the hardware-implemented scheme, the receiver circuit is non-resonant one and simple half-wave rectification has been used as shown in Fig. 4(a). The efficiency for this system can be calculated by eliminating the reactive term involving C_s in equation (25), due to the absence of C_s in the secondary resonance circuit,

$$\eta = \frac{R_{ac}}{((R_{ac} + R_s) + R_P((\omega L_s)^2 + (R_S + R_{ac})^2)/\omega^2 M^2)}. \tag{28}$$

Proposed contactless field power fed BLAC and BLDC system

The complete structure of CPT to the rotor of BLAC and BLDC motors has been shown in Fig. 5. Fig. 6 shows the construction of the CPT scheme with winding design. It provides the facility for
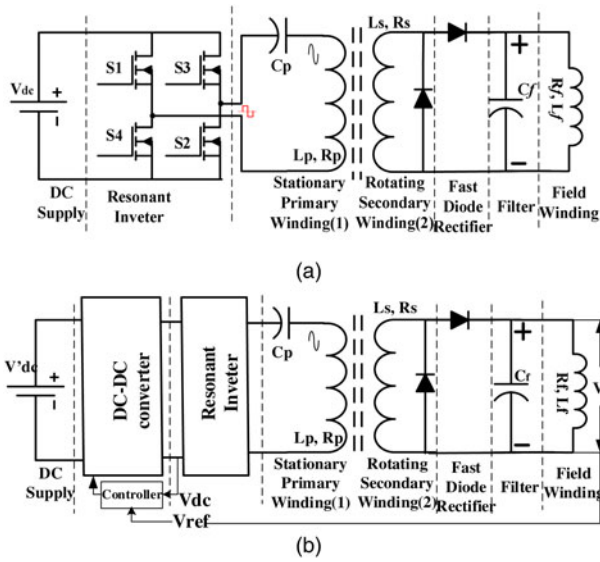
Fig. 4. (a) Resonant inverter supply to series LC resonating branch in primary winding (C_p, L_p, R_p) with a fixed DC source. (b) Scheme of using close-loop controlled DC-DC converters to achieve variable DC supply at the input side of the resonant inverter.

the field power control and DC energy transfer capability to rotor field without any brushed arrangement through wireless electricity transfer principle which works on inductively generated EMF at high frequency.

At any speed of rotation, the DC output voltage at the rotor remains constant. The cylindrical-shaped primary winding made of litz wire in series with a tuning capacitor is fed with the switched DC supply or a high-frequency resonant alternating supply through H-Bridge inverter comprised of high-frequency power electronic switches (RF Power MOSFETs). The secondary helical solenoid winding is mounted on the rotating shaft. Conductors may be stranded or non-stranded. Litz wire is suitable, in a proper frequency range between 50 kHz and 3 MHz [43] for achieving reduced inductance. Litz wire exhibits a lower

value of frequency-dependent winding resistance as compared to solid wires. However, for very high frequency (above 1 MHz), the non-stranded single conductor provides better results and is used in this experimentation for both primary and secondary coils. The voltage at high frequency is induced in the secondary winding due to the transformer action with air core as the medium. High-frequency-induced voltage sets up oscillations in the secondary circuit and the voltage gain to the load is increased at tuning frequency. Following are the main components of the proposed design.

(1) Primary resonant/switch mode winding.
(2) Secondary winding in the rotor with the axis of winding in shaft axis. Winding is situated on a hard hollow cylindrical base.
(3) Capacitor C_f inside the hollow shaft.
(4) Fast diode for high-frequency resonant/switch mode application.
(5) Wound field in the rotor.
(6) Three-phase stator winding.
(7) Stator yoke.
(8) Shaft.
(9) Mechanical load
(10) Bearing
(11) Bearing mounting
(12) High-frequency supply system for primary winding "1" using switch mode or resonant inverter circuit.
(13) Position detection scheme or commutation point detection scheme, e.g. Hall sensors or sensorless.
(14) Commutation logic and PWM generation for current-controlled switching of power electronic switches in VSI/CSI.
(15) VSI or CSI.
(16) DC-DC converter for variable voltage input to the inverter.
(17) Tuning capacitor C_p in the transmitter.

As shown in Fig. 6, the items with serial no. 1–5 together are the new modification to the PMBLDC motor with the necessary implementation of item no. 12. Fig. 6(a) shows the construction of
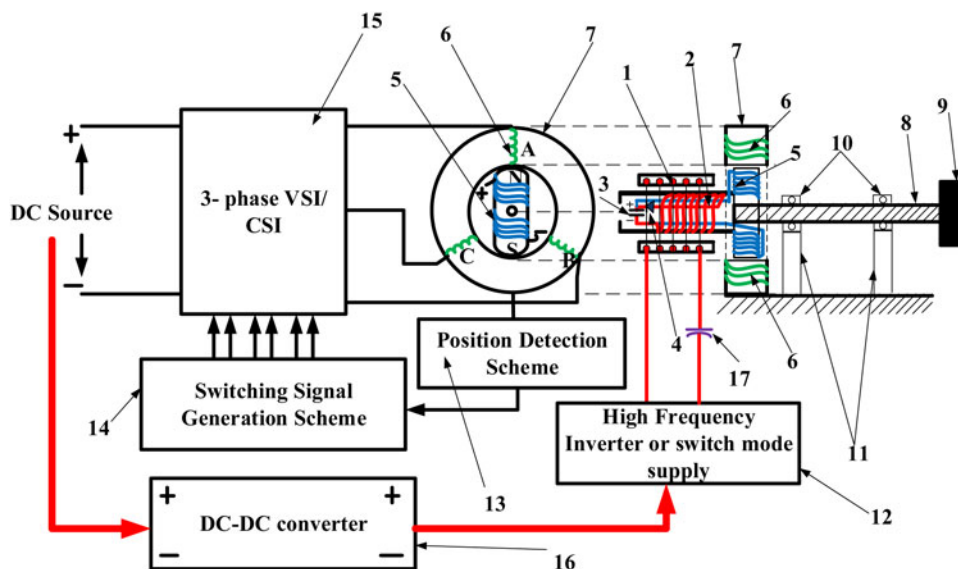

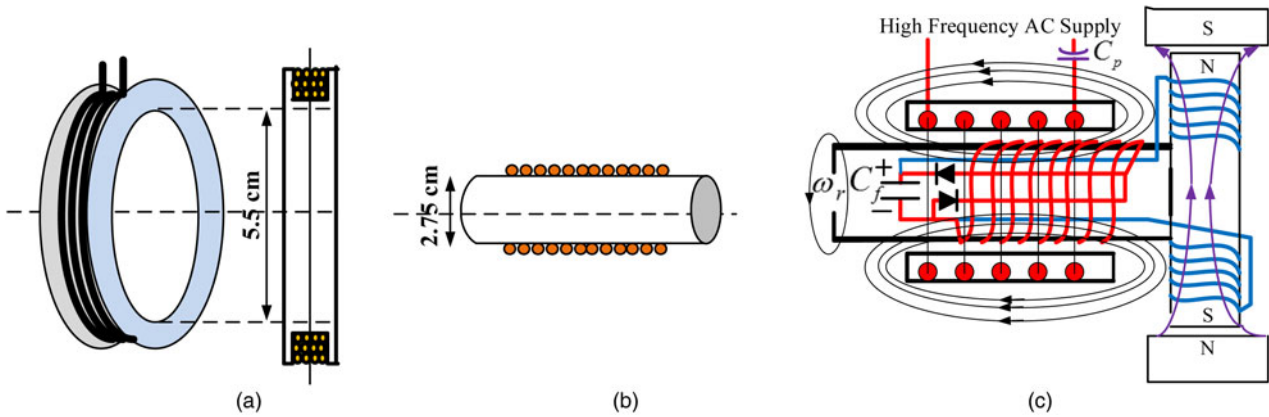**Fig. 5.** Complete brushless DC/AC motor drive system with IPT-based contactless wound rotor field.

Fig. 6. Design of (a) primary stationary winding, (b) secondary or rotating winding, and (c) complete system with primary winding, secondary winding, and field winding.

the transmitter, Fig. 6(b) shows the construction of the receiver circuit, and Fig. 6(c) shows the complete arrangement with connected field winding.

The motional EMF is zero due to fixed axis of windings and only inductively generated voltage (due to transformer action) is present in the secondary winding. In other words, no effect of rotation is imposed on the inductively generated voltage in the secondary, as the secondary winding remains at the same relative position with respect to the stationary winding "1" for any direction and speed of the rotor. Only the conductors virtually move in the longitudinal direction of the shaft relative to the stationary winding and axial flux lines are not cut. The voltage gain depends on input DC voltage given to the resonant inverter "1" and inverter switching frequency, assuming that the equivalent load of the field winding "5" is constant. The air gap between "1" and "2" should be kept minimum, so as to achieve the maximum flux linkage from primary to secondary and maximum efficiency. There is no saturation effect due to the air gap. Flux varies linearly with primary flux.

DC-DC converter "16" facilitates the variation of DC supply voltage feeding the resonant inverter "12" and provides inductively transferred variable DC voltage across the field winding terminals of the rotor. The field flux can be controlled using this variable rotor voltage. The input DC supply to DC-DC converter at source terminals of resonant inverter may be fed from the same or separate DC source as to main VSI. Feeding from the same source gives the shunt field DC motor-type configuration and feeding from a separate source gives the separately excited type of configuration.

The proposed rotor flux control scheme in connection with conventional position detection scheme "13" and rectangular (or quasi-rectangular) current fed phase commutation scheme "14" of stator windings "6" results in contactless wound field BLDC motor configuration. On the other hand, feeding the three-phase stator winding "6" with PWM controlled sinusoidal current wave and using the proposed field flux control scheme provides contactless wound field (permanent magnetless) BLAC configuration.

Proposed hardware setup

A low-power prototype of the proposed system has been initially developed in the Virtual Instrumentation Laboratory of MNNIT Allahabad using a previously developed multiconfiguration stator [46] as shown in Fig. 7. The experiment was carried out connecting
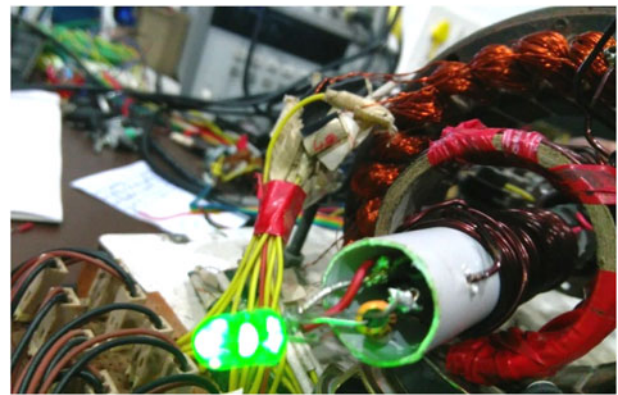

Fig. 7. Test was carried out in the previously developed multiconfiguration stator machine [46]. Concentrated winding of $25\,\mu H$ inductance in primary and helical solenoid coil of $38.5\,\mu H$ in the rotor are used. A green LED is connected to indicate rotor power transfer.

the components $L_p = 25\,\mu H$, $R_p = 0.084\,\Omega$, and $C_p = 6.8\,\mu F$ as per the circuit shown in Fig. 3(a). Secondary winding parameters are $L_s = 38.6\,\mu H$, $R_s = 0.258\,\Omega$ and $C_f = 6.8\,\mu F$. The inductance of the winding was tested using the LCR meter at the setting of 1000 Hz.

In both the windings, a single conductor of size 15 SWG is used in the initial setup. The diameter of the inner hollow rotor coil is 2.75 cm. The diameter of the outer coil is 5.5 cm. The radial separation between the conductors of both windings is 1.375 cm approximately.

The proposed system has been studied with low-voltage low-power input and output. Variable DC output at rotor terminals can be achieved by varying the DC supply to resonant inverter and it is observed that efficiency is maximum when the tuning for maximum voltage has been done. This variable DC output can later be used to vary the field flux in the rotor.

At the first stage of investigation, the no-load output DC voltage developed in the rotor was measured for the circuit configuration shown in Fig. 4(a). The output AC voltage, output DC voltage and input inductor current have been shown for the prototype system in Fig. 8(a). The output AC voltage, input AC voltage and input inductor current have been shown for the prototype system in Fig. 8(b).

The rectangular alternating input voltage applied to LC series resonant primary circuit gives sinusoidal AC voltage. The peak
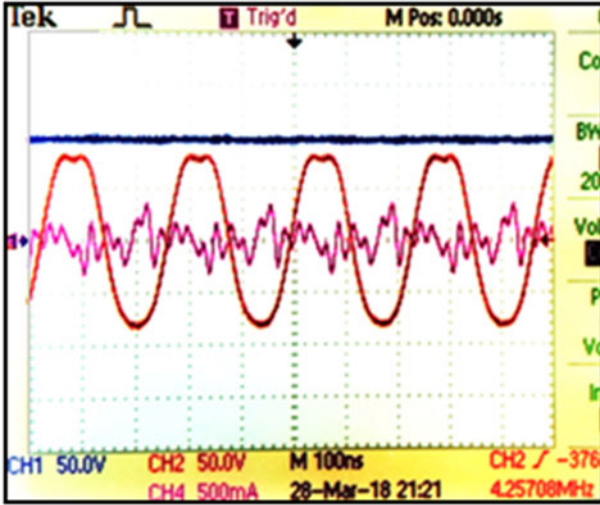
(a)
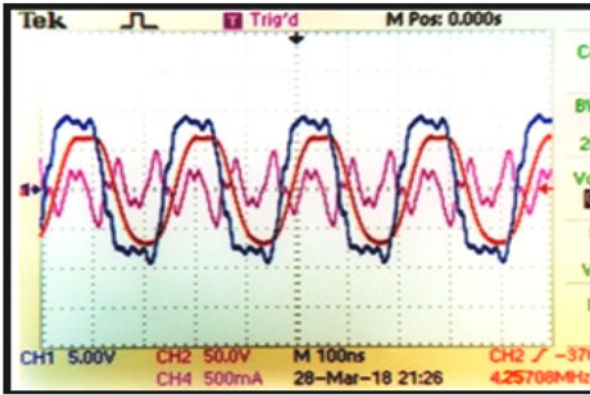
(b)

Fig. 8. Output AC voltage in the rotor (red) 50 V/div, probe 10X, output DC voltage in DC terminals of the rotor (blue) 50 V/div, probe 10X, and input resonant current (pink) with 500 mA/div and 1A/V current probe. Time scale 100 ns/div. (b) Output AC voltage in the rotor (red) 50 V/div, probe 10X, input AC voltage (blue) to RLC branch, 5 V/div, probe 1X, and input resonant current (pink) with 500 mA/div and 1A/V current probe. Time scale 100 ns/div.

magnitude of AC input voltage is kept 9.950 V. Current measurement circuit has the probe ratio of 1 V/A and probe has been set at current. Then, various input frequencies were applied. With the output capacitor of 6.8 μF, the maximum voltage available at rotor terminals is 95 V at 4.25 MHz. Maximum DC output occurs at the open circuit with probe resistance of 10 MΩ. At no load (open circuit), the highest output occurs at 4.25 MHz. Though the probe resistance also affects the highest value attained as the initially designed system is low powered. For 10X setting, probe resistance is 10 MΩ, and at this resistance, the maximum DC voltage is 100 V which occurs at 4.25 MHz.

It is to be noted that, ultra-fast diode SF12 of Multicomp make has been used in real-time for the purpose of rectification and secondary freewheeling. Secondary resonance frequency for the circuit containing C_s and L_s can be given by [47],

$$\omega_s^2 = \frac{1}{L_s C_s}. \qquad (29)$$

Considering the junction capacitance of 30.0 pF of the ultra-fast freewheeling diode SF12 of Multicomp make used in the secondary resonating circuit, the calculated resonance frequency is
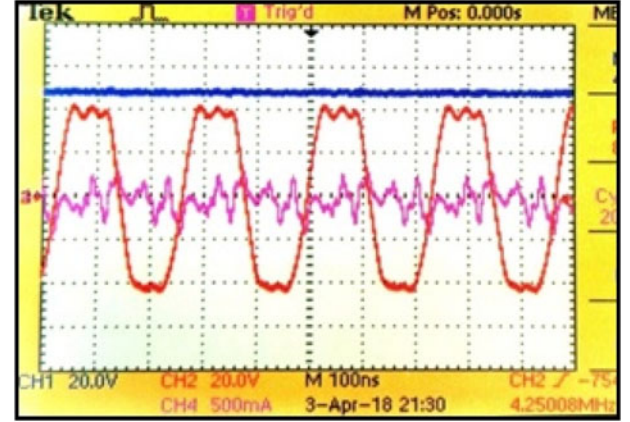

Fig. 9. Output AC voltage (red) in the rotor at 20 V/div, probe 10X, output DC voltage in the DC terminals of the rotor (blue) at 20 V/div, probe 10X, and input resonant current (pink) with 500 mA/div and 1A/V current probe. Time scale 100 ns/div. Maximum DC output at the open circuit was 49.8 V (only 10 MΩ probe resistance).

4.676 MHz which is very close to the actual value of frequency to achieve the maximum voltage in output terminals.

In the next case, an increased value of the output capacitor was used at DC terminals. The maximum value of steady-state open circuit DC output voltage was recorded as 49.8 V for the increased value of the output capacitor (4006.8 μF). In this case, the waveforms of primary inductor voltage, output no-load dc voltage and output ac voltage have been shown in Fig. 9, while switching frequency is kept at 4.25 MHz.

In order to observe the capability of the proposed system for CPT to the rotor at standstill as well as during the rotation at any speed, a light-emitting diode (LED) of green color is connected (Fig. 10) at the DC output terminal in the rotor. No wire to the rotor DC terminals was connected to measure or feed the power. Rectangular alternating square wave voltage 10 Volt was directly fed to the primary coil through the function generator and the output of 3 V was obtained at the output DC terminals of the rotor when LED with a current rating of 20 mA and voltage rating of 2.5–3.5 V is connected. The rotor was rotated by external means at a speed of 500 rpm approximately. Figs. 10(a) and 10(b) show the results in the form of the constant light intensity of LED due to constant power availability to the LED, irrespective of any speed and rotor angle in the proposed prototype.

It is to be noted that the frequency of tuning was different for the loaded condition. The frequency for maximum output at this load was again tuned. The field resistance is practically assumed fixed. The maximum value of LED light intensity occurs at 5.18 MHz as observed from experimentation. The power input, as well as mutual coupling was low and the voltage was sufficient only for LED.

The effect of the gradual variation of frequency on output DC voltage and DC voltage gain has been studied in the proposed system with input RMS voltage of 9.950 V and output capacitance value of 4006.8 μF. It can be observed from Fig. 11 that the switching frequency should be fixed at the point of maximum voltage, i.e. 49.8 V (maximum voltage gain of 5 approximately) and fast boost. This happens at an optimal frequency of 4.25 MHz, which provides the highest efficiency considering the inductor resistance, capacitive ESR and probe resistance as load.

The variation of the output voltage at DC terminals of the receiver with respect to the input voltage to the resonant IPT circuit has been plotted in Fig. 12, while the switching frequency
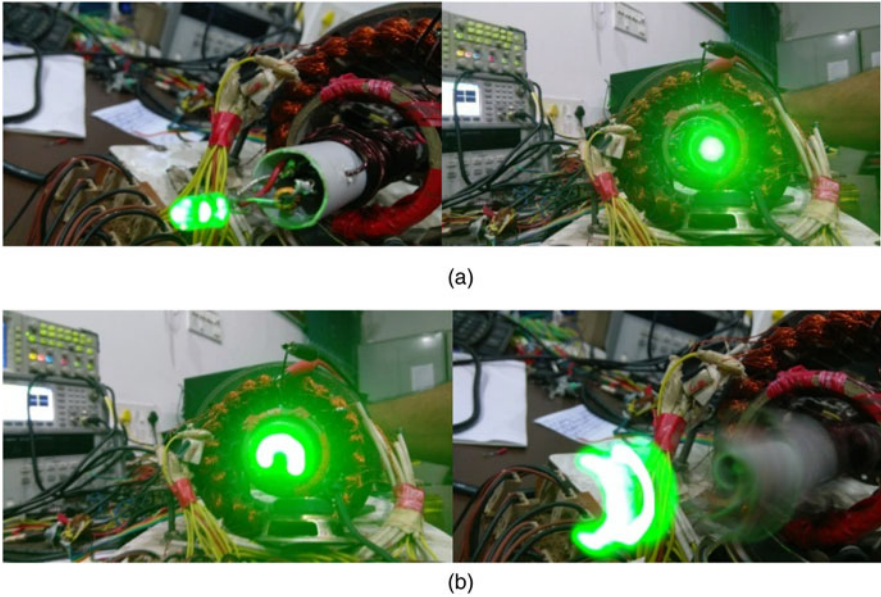
(a)

(b)

Fig. 10. (a) LED light intensity at a stationary rotor. (b) LED light intensity when rotated at approximately 500 rpm.
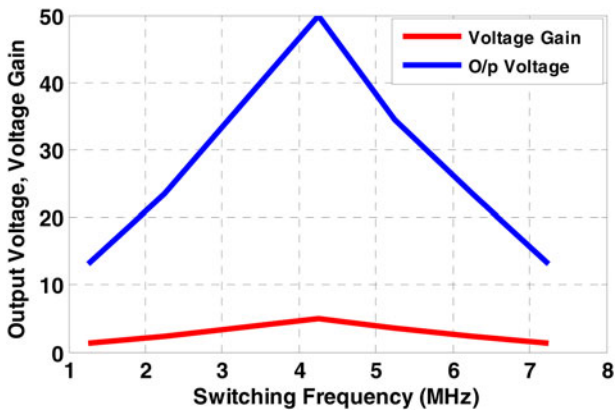

Fig. 11. Variation of rotor output dc voltage and voltage gain (V_o/V_{inrms}) with respect to the variation in the input switching frequency at input rms voltage of 9.950 V_{rms}.
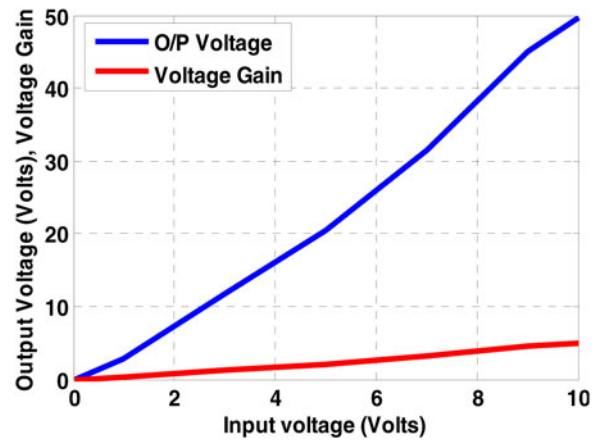

Fig. 12. Variation of no-load rotor output voltage with respect to input RMS voltage at a fixed frequency of 4.25 MHz.

fixed at 4.25 MHz. This shows that the output linearly varies with respect to the input voltage.

Conclusion

Availability of constant field power independent of any rotor angle and rotational speed is a necessary requirement of the rotor field flux in the brushed DC motor, BLDC motor, and BLAC motors. This paper presents an alternative approach for designing the slip-rings that allow the contactless power transfer (CPT) to the rotor of BLDCMs or PMSMs. The above experiment verifies that the power transferred to the rotor with the proposed technique is invariable with the change in the rotor angle and speed. The DC power in the rotor is available at standstill also. The rotor voltage varies proportionally to the DC voltage fed to the resonant inverter. The efficiency and magnitude of power transfer to the rotor can further be increased with various topologies of WPT as well as with the increased inverter frequency with matching parameters. However, power electronics devices together with their drivers have set a limit on the efficiency and magnitude due to limited frequency ranges operating capability. Presently, LED has been used for the indication of the power transfer to the rotor and it can later be substituted with a wound field coil with increased input and output power levels and improved efficiency.

References

1. **Da Costa JP, Pinheiro H, Degner T and Arnold G** (2010) Robust controller for DFIGs of grid-connected wind turbines. *IEEE Transactions on Industrial Electronics* **58**, 4023–4038.

2. **Gao G and Chen W** (2009). Design challenges of wind turbine generators. In *2009 IEEE Electrical Insulation Conference*, IEEE, pp. 146–152.

3. **Hall RD and Roberge RP** (2010) Carbon brush performance on slip rings. In *Conference Record of 2010 Annual Pulp & Paper Industry Technical Conference*, IEEE, pp. 1–6.

4. **IEEE** (1975) *IEEE standard test procedure for carbon brushes*, IEEE Standard 116.

5. **Hurst C** (2010) *China's rare earth elements industry: What can the west learn?*. Institute for the Analysis of Global Security Washington DC.

6. **Ludois DC and Brown I** (2017) *Brushless and permanent magnet free wound field synchronous motors for EV traction* (No. DOE-Wisconsin-6849). University of Wisconsin-Madison, Madison, WI (United States), Final Report 3/31/2017.

7. **Chakraborty C, Basak S and Rao YT** (2017) A new series of brushless and permanent magnetless synchronous machines. In *2017 IEEE 26th International Symposium on Industrial Electronics (ISIE)*, IEEE, pp. 1425–1430.

8. **Landsman EE** (1970) Rotary transformer design. In *1970 IEEE Power Electronics Specialists Conference*, IEEE, pp. 139–152.

9. **Papastergiou KD and Macpherson DE** (2007) An airborne radar power supply with contactless transfer of energy – Part I: rotating transformer. *IEEE Transactions on Industrial Electronics* 54(5), 2874–2884.

10. **Papastergiou KD and Macpherson DE** (2007) An airborne radar power supply with contactless transfer of energy – Part II: converter design. *IEEE Transactions on Industrial Electronics* 54(5), 2885–2893.

11. **Legranger J, Friedrich G, Vivier S and Mipo JC** (2007) Comparison of two optimal rotary transformer designs for highly constrained applications. In *2007 IEEE International Electric Machines & Drives Conference*, vol. 2, IEEE, pp. 1546–1551.

12. **Tartibi M and Domijan A** (1996) Optimizing ac-exciter design. *IEEE Transactions on Energy Conversion* 11(1), 16–24.

13. **Gomes DR and Chabu IE** (2010) Studies on electrical stresses in rotating rectifiers for brushless exciters. In *2010 9th IEEE/IAS International Conference on Industry Applications-INDUSCON 2010*, IEEE, pp. 1–6.

14. **Dillman TL, Skooglund JW, Keay FW, South WH and Raczkowski C** (1971) A high initial response brushless excitation system. *IEEE Transactions on Power Apparatus and Systems* PAS-90(5), 2089–2094.

15. **Allen GFH** (1975) Brushless excitation systems for synchronous machines. *Electronics and Power* 21(15), 866–869.

16. **Veszpremi K** (2004) Comprehensive optimization of brushless excitation of synchronous machine. In *30th Annual Conference of IEEE Industrial Electronics Society, 2004. IECON 2004*, vol. 2, IEEE, pp. 1327–1332.

17. **IEEE** (2007) IEEE standard definitions for excitation systems for synchronous machines, IEEE Standard 421.1.

18. **Wrobel R, Griffo A, Mlot A, Yon J, Mellor P, Turner J and Collins R** (2011) Design study of a three-phase brushless exciter for aircraft starter/generator. In *2011 IEEE Energy Conversion Congress and Exposition*, IEEE, pp. 3998–4004.

19. **Marx SH and Bounds RW** (1971) A kilowatt rotary power transformer. *IEEE Transactions on Aerospace and Electronic Systems* AES-7(6), 1157–1163.

20. **Papastergiou KD, Macpherson DE and Fisher F** (2005) A 1 kW phase-shifted full bridge converter incorporating contact-less transfer of energy. In *2005 IEEE 36th Power Electronics Specialists Conference*, IEEE, pp. 83–89.

21. **Jun LC, Ming Q and Bin ZJ** (2008) Modeling and test of contactless transformer used in inductosyn. In *2008 International Conference on Electrical Machines and Systems*, IEEE, pp. 4323–4327.

22. **Smeets JPC, Encica L and Lomonova EA** (2010) Comparison of winding topologies in a pot core rotating transformer. In *2010 12th International Conference on Optimization of Electrical and Electronic Equipment*, IEEE, pp. 103–110.

23. **Moradewicz AJ and Kazmierkowski MP** (2009) High efficiency contactless energy transfer system with power electronic resonant converter. *Bulletin of the Polish Academy of Sciences: Technical Sciences* 57(4), 375–381.

24. **Abdolkhani A and Hu AP** (2011) A novel detached magnetic coupling structure for contactless power transfer. In *IECON 2011–37th Annual Conference of the IEEE Industrial Electronics Society*, IEEE, pp. 1103–1108.

25. **Abdolkhani A and Hu A** (2011) A sandwiched magnetic coupling structure for contactless slipring applications. *International Geoinformatics Research and Development* 2, 8.

26. **Colonel W, McLyman T and Landsman E** (2011) Rotary transformer design, pp. 19.1–19.10.

27. **Potter BA and Shirsavar SA** (2006) Design, implementation and characterisation of a contactless power transfer system for rotating applications. In *IECON 2006-32nd Annual Conference on IEEE Industrial Electronics*, IEEE, pp. 2168–2173.

28. **Pedder DA, Brown AD and Skinner JA** (1999) A contactless electrical energy transmission system. *IEEE Transactions on Industrial Electronics* 46, 23–30.

29. **Hu AP** (2001) *Selected Resonant Converters for IPT Power Supplies* (Doctoral dissertation). ResearchSpace@ Auckland.

30. **Lu M, Bagheri M, James AP and Phung T** (2018) Wireless charging techniques for UAVs: a review, reconceptualization, and extension. *IEEE Access* 6, 29865–29884.

31. **Barman SD, Reza AW, Kumar N, Karim ME and Munir AB** (2015) Wireless powering by magnetic resonant coupling: recent trends in wireless power transfer system and its applications. *Renewable and Sustainable Energy Reviews* 51, 1525–1552.

32. **Lu X, Wang P, Niyato D, Kim DI and Han Z** (2014) Wireless networks with RF energy harvesting: a contemporary survey. *IEEE Communications Surveys & Tutorials* 17, 757–789.

33. **Roes MG, Duarte JL, Hendrix MA and Lomonova EA** (2012) Acoustic energy transfer: a review. *IEEE Transactions on Industrial Electronics* 60(1), 242–248.

34. **Ying W, Luguang Y and Shangang X** (2005) Modeling and performance analysis of the new contactless power supply system. In *2005 International Conference on Electrical Machines and Systems*, vol. 3, IEEE, pp. 1983–1987.

35. **Covic GA and Boys JT** (2013) Inductive power transfer. *Proceedings of the IEEE* 101(6), 1276–1289.

36. **Kurs A, Karalis A, Moffatt R, Joannopoulos JD, Fisher P and Soljačić M** (2007). Wireless power transfer via strongly coupled magnetic resonances. *Science* 317(5834), 83–86.

37. **Aditya K and Williamson SS** (2014) Comparative study of Series-Series and Series-Parallel compensation topologies for electric vehicle charging. In *2014 IEEE 23rd International Symposium on Industrial Electronics (ISIE)*, IEEE, pp. 426–430.

38. **Chopra S and Bauer P** (2011) Analysis and design considerations for a contactless power transfer system. In *2011 IEEE 33rd International Telecommunications Energy Conference (INTELEC)*, IEEE, pp. 1–6.

39. **Pellitteri F, Boscaino V, Di Tommaso AO, Miceli R and Capponi G** (2013) Inductive power transfer for 100W battery charging. In *IECON 2013-39th Annual Conference of the IEEE Industrial Electronics Society*, IEEE, pp. 894–899.

40. **Wang CS, Covic GA and Stielau OH** (2001) General stability criterions for zero phase angle controlled loosely coupled inductive power transfer systems. In *IECON'01. 27th Annual Conference of the IEEE Industrial Electronics Society (Cat. No. 37243)*, vol. 2, IEEE, pp. 1049–1054.

41. **Wang CS, Stielau OH and Covic GA** (2005) Design considerations for a contactless electric vehicle battery charger. *IEEE Transactions on Industrial Electronics* 52(5), 1308–1314.

42. **Rituraj G, Kushwaha BK and Kumar P** (2018) Contactless power transfer system for sealed lead acid battery charging. *Wireless Power Transfer* 5(1), 20.

43. **Piri M, Špánik P, Frivaldský M and Kondelova A** (2016) Wireless (power transfer) transmission of electrical energy (electricity) intended for consumer purposes up to 50 W. *Advances in Electrical and Electronic Engineering* 14(1), 40–48.

44. **Trevisan R and Costanzo A** (2014) State-of-the-art of contactless energy transfer (CET) systems: design rules and applications. *Wireless Power Transfer* 1(1), 10–20.

45. **Vandevoorde G and Puers R** (2001) Wireless energy transfer for stand-alone systems: a comparison between low and high power applicability. *Sensors and Actuators A: Physical* 92(1-3), 305–311.

46. **Soni UK and Tripathi RK** (2017) Two phase bipolar and two phase split unipolar operation of PMSM with multiconfiguration stator using

LABVIEW. In *2017 4th International Conference on Power, Control & Embedded Systems (ICPCES)*, IEEE, pp. 1–6.

47. **Jiang B, Wang JG, Chen LJ, Wang B and Wang Q** (2014) A efficient control method for series-parallel CPT system. in 2014 33rd, *Chinese Control Conf. (CCC)*, Nanjing, China, pp. 3500–3504.

Umesh Kumar Soni has obtained B.E. degree from JEC Jabalpur (MP), India in 2003. He has 3 years of industrial experience and more than 4 years of academic experience. He has completed his M.E. in 2011 in control system specialization from JEC, Jabalpur. Presently, he is purusing the Ph.D. degree from MNNIT Allahabad, India and has just submitted his PhD thesis in July 2020 with specialization in power electronics and drives control. His interests include control, robotics, fuzzy, neuro-fuzzy, image processing, renewable energy harvesting, solar and microbial fuel cells, wind power system, microgrids, power electronic converters control, DC-DC PFC and boost converters, bidirectional converters, multilevel inverters, resonant converters, wireless electricity and high speed superefficient motor control.

Prof. Ramesh Kumar Tripathi has obtained the Bachelor degree in Engineering from REC Durgapur, West Bengal in 1989, M.Tech. degree from IT-BHU, Varanasi in 1991, and Ph.D. degree from IIT Kanpur in 2002. He is a Fellow IE and a senior member of IEEE. Presently, he is working as a Professor in the Department of Electrical Engineering, MNNIT Allahabad, India. He has about 30 years of academic experience. He has many research publications in journals and conferences of international repute. His research interests are power electronics switch-mode rectifiers and power supplies, high gain DC-DC Converters, renewable energy harvesting, microbial fuel cells, solar and wind energy, microgrids, magnet load power supplies, power factor correction, electrical drives, power quality and active power filters, and virtual instrumentation.